ROYAL SOCIETY
OF CHEMISTRY

EDGE ARTICLE

Check for updates

All publication charges for this article have been paid for by the Royal Society of Chemistry

An expeditive and green chemo-enzymatic route to diester sinapoyl-L-malate analogues: sustainable bioinspired and biosourced UV filters and molecular heaters†

Benjamin Rioux, [iD] ‡[a] Louis M. M. Mouterde, [iD] ‡[a] Jimmy Alarcan,‡[b]
Temitope T. Abiola, [iD] ‡[cd] Matthias J. A. Vink, [iD] ‡[e] Jack M. Woolley, [iD] ‡[c]
Aurélien A. M. Peru,[a] Matthieu M. Mention,[a] Fanny Brunissen,[a] Giel Berden, [iD] [e]
Jos Oomens, [iD] *[e] Albert Braeuning,*[b] Vasilios G. Stavros [iD] *[cf] and Florent Allais [iD] *[a]

Sinapoyl malate, naturally present in plants, has proved to be an exceptional UV filter and molecular heater for plants. Although there are nowadays industrially relevant sustainable synthetic routes to sinapoyl malate, its incorporation into certain cosmetic formulations, as well as its adsorption on plant leaves, is limited by its hydrophilicity. To overcome these obstacles, it is important to find a way to effectively control the hydrophilic–lipophilic balance of sinapoyl malate to make it readily compatible with the cosmetic formulations and stick on the waxy cuticle of leaves. To this end, herein, we describe a highly regioselective chemo-enzymatic synthesis of sinapoyl malate analogues possessing fatty aliphatic chains of variable length, enabling the lipophilicity of the compounds to be modulated. The potential toxicity (*i.e.*, mutagenicity, carcinogenicity, endocrine disruption, acute and repeated-dose toxicity), bioaccumulation, persistence and biodegradability potential of these new analogues were evaluated *in silico*, along with the study of their transient absorption spectroscopy, their photostability as well as their photodegradation products.

1. Introduction

Solar radiation supplies light, ultraviolet radiation (UVR), warmth, and energy needed to support life in biological systems, including plants. Although UVR is essential to plant development, it is also harmful if the plant is overexposed to it.[1,2] Indeed, UV wavelengths (100–400 nm), which are the most energetic rays from solar emission reaching the surface of the Earth, can disrupt the photosynthetic machinery, especially because they are responsible for the generation of reactive oxygen species (ROS), examples being $O_2^{\cdot-}$, H_2O_2, $HO^{\cdot}$, $^1O_2$.[3–5]

Although they are known to be reactive towards lipids, proteins and DNA, these entities have been shown to play a role in cellular events (*e.g.*, proliferation, differentiation, metabolic adaptation).[6–8] When ROS are generated, their levels in the aforementioned matrices increase leading to the dysfunction of the general homeostasis.[6] To avoid these detrimental processes, plants have developed biosynthetic pathways leading to metabolites that can absorb UVR as natural UV filters, that also act as free radical scavengers.

Phenylpropanoids are prominent amongst UV filters; plants can biosynthesize flavonoids or *p*-hydroxycinnamic acid derivatives in their leaves.[9–11] *p*-Hydroxycinnamic acid derivatives, notably the sinapate ester sinapoyl-L-malate (SM), function as sunscreen molecules in thale cress (*Arabidopsis thaliana*).[12,13] When overexposed to UVR, the biosynthesis of sinapate esters, mediated *via* the phenylpropanoid pathway,[10] is upregulated to accumulate the latter into the vacuoles of cells in the upper epidermis of leaves, thus increasing UVR protection.[2,13–15] Sinapate esters were identified as being able to dissipate excess energy, accumulated from exposure to UVR, as heat.[16–18] Very recently, Abiola *et al.* highlighted the ability of some *p*-hydroxycinnamic acid derivatives to convert light to heat, *i.e.*, photothermal effect.[18] This insight is paving the way for a new generation of UV filters with antioxidant and photothermal properties that would be advantageous in cosmetics as well as

[a]*URD Agro-Biotechnologies Industrielles (ABI), CEBB, AgroParisTech, 51110, Pomacle, France. E-mail: florent.allais@agroparistech.fr*

[b]*Department of Food Safety, German Federal Institute for Risk Assessment, Max-Dohrn-Str. 8-10, 10589, Berlin, Germany. E-mail: albert.braeuning@bfr.bund.de*

[c]*Department of Chemistry, University of Warwick, Gibbet Hill Road, CV4 7AL, Coventry, UK. E-mail: v.stavros@warwick.ac.uk*

[d]*Department of Chemistry, Lash Miller Chemical Laboratories, 80 St. George Street, Toronto, ON, M5S 3H6, Canada*

[e]*Institute for Molecules and Materials, FELIX Laboratory, Radboud University, Toernooiveld 7, 6525ED, Nijmegen, Netherlands. E-mail: j.oomens@science.ru.nl*

[f]*School of Chemistry, University of Birmingham, Edgbaston, Birmingham B15 2TT, UK. E-mail: v.stavros@bham.ac.uk*

† Electronic supplementary information (ESI) available. See DOI: https://doi.org/10.1039/d3sc04836e

‡ These authors contributed equally to this work.

Fig. 1 Structures of sinapoyl-L-malate (SM) and its biobased fatty esters derivatives synthesized and studied in this work.

plant and crop protection. For example, sinapate esters incorporated in a foliar spray could supplement the natural UVR protection against overexposure to UVR as well as scavenging ROS. In addition, the generated heat would provide thermal energy to the biological system allowing successful crop growth in cooler geographical regions and offering protection against sudden daytime frost damage. Frost damage alone is estimated to cost Europe €3.3 billion per annum in reduced harvests. Although naturally occurring SM could be a good candidate for such an application, its solubility in water makes it easily washable by the rain, rendering its effectiveness dependent on the weather. Therefore, developing molecules that interact with, say, the waxy cuticle of the plant leaves, would be a tantalising prospect towards realising the aforementioned application.

In the quest for new and innovative bioactive compounds, Nature is a formidable source of inspiration for research scientists. Building on SM, biomimetics is a powerful strategy to design *de novo* biobased and bioinspired UV filters,[19] with SM (and derivatives thereof) the front-runner to replacing petrosourced UV filters – such as avobenzone, octocrylene, oxybenzone or Octinoxate™ – which have been banned for use in cosmetic products on some pacific islands like Hawaii because of their toxicity to coral reef (*i.e.*, bleaching, toxic degradation products).[20–24] Moreover, the carbon footprint of humans on Nature must be drastically reduced. Thus, the use of biobased compounds instead of their petroleum-based counterparts is not only highly sought after, but also crucial for the environment. It is therefore essential to use (bio)synthetic processes with low ecological impacts inspired by the Green Chemistry Principles.[25]

In this context, the valorization of agricultural coproducts and waste, such as lignin and lignans, appears as an exceptional source of natural and sustainable building blocks and allows one to obtain *p*-hydroxybenzaldehydes (*i.e.* vanillin, syringaldehyde)[26,27] that can give access to a countless number of biobased compounds with a wide range of properties, such as antioxidant,[28–30] anti-UV,[31–35] antimicrobial,[36–38] anticancer,[39–41] anti-inflammatory,[42–44]

antiviral,[45–47] as well as anti-tyrosinase activities.[48–50] *p*-Hydroxycinnamic acid derivatives can be readily obtained through the Knoevenagel and Knoevenagel–Doebner condensations of the corresponding *p*-hydroxybenzaldehydes. These two condensation reactions, that involve the use of pyridine as solvent and aniline or piperidine as amine catalysts,[51] have been known for more than a century and many procedures were published highlighting several major advancements using green procedures such as reducing reaction times with microwave activation,[52,53] non-hazardous solvents[54–56] or catalysts.[57–59] Recently, more sustainable synthetic pathways were described with the catalyst-free Knoevenagel condensation in water[30,33,60] and the proline-mediated Knoevenagel–Doebner condensation in ethanol.[36,61,62]

In the present work, starting from natural and sustainable syringaldehyde, and according to the aforementioned sustainable Knoevenagel–Doebner condensation, we have developed a new generation of eight biobased SM derivatives, bearing fatty chains (Fig. 1) to enhance their hydrophobic interactions with the waxy cuticle of leaves, as well as to facilitate their formulations for sunscreen applications. To evaluate the potential of these novel lipophilic compounds as molecular heaters or alternatives to current petroleum-based UV-filters, we have (i) investigated the photophysical properties of SM derivatives using steady-state and ultrafast transient absorption spectroscopies to gain insight into the light-to-heat generating pathways, (ii) explored the photodegradation of dioctyl sinapoyl-L-malate (DOSM, the most promising of the SM derivatives tested) and its byproducts formation, and (iii) studied the environmental impact and potential toxicity on human of all compounds through *in silico* approaches.

2. Experimental

2.1. General

All reagents were purchased from Sigma-Aldrich, TCI, Merck or VWR and used as received. Solvents were purchased from

Thermo Fisher Scientific and VWR. Deuterated dimethyl sulfoxide (DMSO-d_6 < 0.02% H_2O), acetone (acetone-d_6 < 0.02% H_2O) and chloroform (CDCl$_3$-d < 0.02% H_2O) were purchased from Euriso-top. Immobilized *Candida antarctica* lipase B (Novozym® 435, N435, 10 000 PLU per g) was obtained from Univar Solutions SAS.

2.2. NMR analyses

NMR spectra were recorded on a Bruker Fourier 300 (Billerica, MA, USA). ^{1}H NMR spectra were recorded in DMSO-d_6 (residual peak at δ = 2.50 ppm), acetone-d_6 (residual peak at δ = 2.05 ppm) or chloroform-d (residual peak at δ = 7.26 ppm) at 300 MHz. Chemical shifts were reported in parts per million relatives to the solvent residual peak. Data are reported as follows: integration, chemical shift (δ ppm), multiplicity (s = singlet, d = doublet and dd = doublet of doublets), coupling constant (Hz) and assignment. ^{13}C NMR spectra of samples were recorded at 75 MHz in DMSO-d_6 (residual signal at δ = 39.52 ppm), acetone-d_6 (residual peaks at δ = 29.82 and 206.03 ppm) or chloroform-d (residual peak at δ = 77.06 ppm). Data are reported as follows: chemical shift (δ ppm) and assignment. All ^{1}H and ^{13}C NMR spectra are available in the ESI (Fig. S1–S16†).

2.3. HRMS analyses

High-resolution mass spectrometry (HRMS) was performed on an Agilent Technologies 1290 system, equipped with a 6545 Q-TOF mass spectrometer (Wilmington, DE, USA) and a PDA UV detector. The source was equipped with a JetStream electrospray ionisation ESI probe operating at atmospheric pressure. HRMS spectra are reported in the ESI (Fig. S17–S24†).

2.4. UV-filtering property and photostability

UV/visible absorption spectra of SM derivatives in ethanol were recorded using a UV/visible Cary 60 Agilent Technologies spectrometer at a concentration of 10 μM. For the photostability study, samples (20 μM, EtOH) were irradiated for 1 hour with a Rayonet© RPR-200 (λ = 300 nm, P = 8.32 W m^{-2}, stirring, T = 35 °C) using 14 RPR-3000A lamps (SNE Ultraviolet Co Branford Ct USA RPR-3000A). UV spectra were subsequently recorded and the absorbance loss was calculated as a percentage at the λ_{max}. UV photostability spectra are reported in the ESI (Fig. S25–S32†).

2.5. Antiradical activities

Antiradical activities of the SM derivatives were determined *via* 2,2-diphenyl-1-picrylhydrazyl (DPPH) assay. These tests involve adding potential antiradical molecule solution in ethanol at different concentrations to homogeneous DPPH solution. The study was performed under stirring for 7 h 25 min on the following concentrations: 400, 200, 100, 50, 25, and 12.5 μM. Every 5 min, the absorbance was measured at 520 nm. In the end, the percentage curves of DPPH (blue) and reduced DPPH (green) were plotted in Regressi® software using an average of the last six points. The amount needed to reduce the initial number of DPPH free radicals by half (*i.e.*, EC$_{50}$) is provided by the crossing point of %DPPH (blue) and %reduced DPPH

(green). Antiradical measurement spectra are reported in the ESI (Fig. S33–S43†).

2.6. Specific optical rotatory power

Optical activities of the SM derivatives were determined in methanol (or ethanol for dioleylyl derivative of SM) at 0.02 g mL^{-1} on a Bellingham + Stanley ADP410 single wavelength polarimeter.

2.7. Transient absorption spectroscopy

The femtosecond (fs) transient electronic absorption spectroscopy setup used to explore the photodynamics of the SM derivatives in solution has been detailed previously,[31,35,63–65] and only information specific to the present experiments is reported here. Separate samples of SM derivatives were prepared to 1 mM concentration in an oil-based solvent, caprylic capric triglyceride, to enhance the solubility. In all cases, the pump excitation wavelength was chosen to match the relevant λ_{max}. The sample was delivered through a demountable Harrick Scientific flow-through cell equipped with two CaF$_2$ windows separated by 100 μm polytetrafluoroethylene (PTFE), thereby defining the optical path length of the sample. The samples were circulated using a diaphragm pump (SIMDOS, KNF) recirculating from a 25 mL sample reservoir to ensure each pump-probe pulse interacts with a fresh sample, with a maximum pump-probe delay of 2 nanoseconds (ns). The collated spectra reflect changes in optical density (ΔOD) and are chirp corrected for visual purposes using the KOALA software program.[66] To gain insight into the dynamical process following photoexcitation and extract the excited state kinetic information from the TEA spectra obtained for each molecule, a global sequential fitting procedure $(A \xrightarrow{\tau_1} B \xrightarrow{\tau_2} C \xrightarrow{\tau_3} D \ldots)$ implemented through the Glotaran software package was employed.[67,68]

2.8. LC-MS-IRIS study on solar degradation product of DOSM

2.8.1. Sample irradiation.
To evaluate the photostability of DOSM and digeranyl sinapoyl-L-malate (DGSM), we dissolved each photomolecular heater separately in a mixture of MeOH and water (80/20; v/v%) since neither compound would completely dissolve in water alone at a concentration of 10 mM. Solutions were transferred to a custom tubular quartz-topped cuvette, filling it to about 70% of the total volume to ensure that photooxidative reactions can also contribute to degradation. To minimize thermal degradation, which is unrealistic under the natural conditions of applying the photomolecular heaters, we placed the cuvette in a temperature-controlled sample holder at 18.5 °C. This also prevented solvent condensation on the quartz window during the 7 h solar irradiation. An ABET Technologies Sun 2000 simulator irradiated the sample. The simulator's output power and spectral characteristics can be found in Fig. S44.† Simulation conditions are based on the Reference Air Mass 1.5 Spectrum (AM 1.5), corresponding to the sunlight expected at solar noon in Southern Europe at sea level[69,70] and commonly used as a standard for characterizing photovoltaic devices. These conditions are harsher than

expected in the proposed application of photomolecular heaters and are regarded as a worst-case scenario to test the stability of the heaters. During the simulated solar irradiation, the DOSM and DGSM compounds remained dissolved entirely in the MeOH/water mixture. Relative to the field trial tests, this "*in vitro*" experiment allows us to observe the degradation products in the absence of the biological matrix, simplifying the search for byproducts. To characterize the degradation products, 15 μL of the irradiated solution was transferred to an LC-MS sample vial, to which 745 μL of MeOH was added, producing a 20 μM 'degraded' DOSM and DGSM solution. For LC-MS characterization, the non-irradiated 'stock' solution of DOSM and DGSM were diluted similarly to serve as negative controls.

2.8.2. Field trial. Large-scale field trials were conducted for DGSM. To this end, we developed a specific formulation to apply DGSM on leaves tested on grape leaves, as the MeOH and water mixture is unsuitable for crop application. This formulation contains 5% DGSM by weight and was used for field trials on newly grown lettuce, cucumber, tomato, wheat, and sugar beet crops and sprayed at 2.5 L ha^{-1}. After 48 h, a rectangular piece of leaf is cut out for extraction with a total surface area of approximately 20 cm^2. The leaf segment is placed in a 15 mL tube with 5 mL MeCN for extraction on a shaker table for 16 h. After filtering the extract through a 0.2 μm cellulose filter, it is stored in brown glass vials at a temperature of 5 °C until it can be analyzed using LC-MS. This extraction method is more suitable than Soxhlet extraction using MeOH, which we found to compromise the stability of DOSM and DGSM. We collected four replicates from distinct plots across all crops of treated and untreated plots.

2.8.3. LC-MS. For the characterization and fractionation of degradation products, a Bruker Elute HPLC system consisting of an autosampler, column oven, and a Bruker AmaZon Quadrupole Ion Trap (QIT) Mass Spectrometer was operated. A 2.1 × 150 mm Waters Acquity UPLC HSS T3 reversed-phase C18 column with 1.8 μm particles and a 100 Å pore size was utilized for separation. The column was held at 40 °C during separation, and injections of 2 μL were performed while the samples were conditioned to 4 °C. Elution was performed under a linear gradient using solvent A (water) and solvent B (MeOH), both containing 0.1% formic acid (FA). The gradient starts at 95% solvent A and linearly falls to 5% solvent A in 12 min. The 95% solvent B ratio is then maintained for an additional 5 min and subsequently reverted to the initial conditions in 2 min. These initial conditions are maintained for 4.5 min for re-equilibration of the column before a new injection is performed.

We used the QIT-MS to determine elution times of features of interest for degradation product fractionation. The divert valve was programmed to temporarily store the effluent for the InfraRed Ion Spectroscopy (IRIS) experiment by diverting the flow at the observed elution time into an LC vial or 80 μL sample loop. The LC vial was used to allow spiking the sample with a CsCl solution to study the cesium adducts of the molecules of interest, where the sample loop was backflushed into the MS using a syringe pump for IRIS using a Hamilton 250 μL syringe.[71,72]

2.8.4. IRIS measurements. The IRIS measurements were performed on a modified QIT-MS (Bruker AmaZon Speed ETD), which allows for optical access to the trapped ion population by the IR beam of the Free Electron Laser for Infrared eXperiments (FELIX).[73] The modifications also allow the QIT sequence to synchronize with the FELIX laser pulse train. The ion of interest is m/z-isolated in the QIT after directly infusing either the standard or the fractionated sample. The FELIX IR frequency is scanned across the 550–1850 cm^{-1} spectral range in steps of 3–5 cm^{-1}. A mass spectrum records the degree of InfraRed Multiple-Photon Dissociation (IRMPD) induced at each frequency step. To reconstruct the IR spectrum of the mass-isolated ion, we plot the IR-induced photodissociation yield or precursor ion depletion, defined in eqn (1) and (2), respectively, as a function of IR frequency.[74]

$$\text{Yield}(\lambda) = -\ln\left(\frac{I_{P_1}}{I_{P_1} + \sum I_F}\right) \tag{1}$$

$$\text{Depletion}(\lambda) = -\ln\left(\frac{I_{P_1}}{I_{P_0}}\right) \tag{2}$$

Here, I_{P_1} is the intensity of the precursor ion and $\sum I_F$ is the sum of all IRMPD-induced fragments; if no fragments are observed, *e.g.*, because they fall below the low-mass cut-off of the QIT, we use eqn (2), where I_{P_0} is the precursor ion intensity without IR irradiation. To obtain the IR ion spectrum of the synthesized di-octyl-2-hydroxy succinate (DO2HS) external reference standard synthesized in-house, a 10 mM solution of DO2HS was made in a mixture of MeOH and water (80/20; v/v%), which was further diluted in MeOH containing 10% FA to a concentration of 30 μM. A similar procedure was followed for the di-geraniol-2-hydroxy succinate (DG2HS) external reference standard, also synthesized in-house.

2.9. *In silico* toxicology

An important aspect in the development of new bioactive compounds is the investigation of their potential toxicity and fate in the environment. In an early stage of development, *in silico* tools constitute a good strategy to gain initial information and screen potential lead molecules without the use of expensive and time-consuming animal testing. Based on experimental data and the relationships between structure and activity, *in silico* models allow not only predictions for known compounds (*e.g.* filling of data gaps), but also virtual compounds (*i.e.*, not yet synthesized).[75–77]

2.9.1. Mutagenicity and carcinogenicity. The different software tools VEGA,[77] TEST[78] and LAZAR[79] were used for the prediction of mutagenicity and carcinogenicity. The use of multiple models has proven to increase the predictive power.[80,81] Detailed information on the use of these models can be found in our previous works.[18,30] Briefly, the predictions generated from the different models were converted to numeric values between 0 and 1, in which presumable non-mutagenicity/non-carcinogenicity ranges from 0 to 0.50, while mutagenicity/carcinogenicity ranges from 0.51 to 1 (see Table S1†).

The arithmetic mean of the different generated prediction scores was calculated and plotted in a diagram, divided into three zones according to the overall predictions: a score higher than 0.66 means a positive prediction (mutagenic/carcinogenic) with good reliability, while a score lower than 0.33 means a negative prediction (mutagenic/carcinogenic) with good reliability. A score between 0.33 and 0.66 is considered equivocal. This includes the score range between 0.33 and 0.5, which is regarded as a negative prediction (not persistent) with insufficient reliability, as well as the score range between 0.5 and 0.66, regarded as a positive prediction (persistent) with insufficient reliability.

2.9.2. Endocrine toxicity. The possible endocrine toxicity of the test compounds was investigated using the VEGA platform. Different models are available in VEGA and provide a qualitative prediction (yes/no): there are four models for receptor-mediated effects (*i.e.*, estrogen receptor-mediated effect IRFMN/CERAPP, androgen receptor-mediated effect IRFMN/COMPARA, thyroid receptor alpha effect NRMEA, and thyroid receptor beta effect NRMEA), and one model for binding affinity (estrogen receptor relative binding affinity model IRFMN). Additional information about the reliability of the prediction (low, moderate, or high reliability) is provided for each model in the ESI section.†

2.9.3. Acute and repeated-dose toxicity. Acute toxicity was evaluated by estimating the oral LD_{50} in rats. Prediction was made using TEST consensus model based on a dataset comprising values from 7413 substances. Besides, repeated-dose toxicity was evaluated by estimating a 90 day toxicity study's no-observed-adverse-effect level (NOAEL) using the module NOAEL – IRFMN/CORAL provided by the VEGA platform. The model is based on a dataset comprising values from repeated-dose 90 day oral toxicity studies in rodents with 140 substances.

2.9.4. Bioaccumulation. The bioconcentration factor (BCF) is defined as the ratio of the concentration of the test chemical in aquatic organisms to its concentration in the ambient environment. It is employed to evaluate the bioaccumulation potential of test compounds. We used both the VEGA and ISIDA[82] platforms to predict the BCF. VEGA provides 4 models (CAESAR, Meylan, KNN/Read-across, and Arnot-Gobas) allowing the determination of a log value, plus information about the reliability of the prediction (low, moderate, or high). ISIDA is a consensus regression model based on 17 individual models. The outcome is given as a log value with a prediction confidence estimate (outside applicability domain (AD), average, good, and optimal). The Registration, Evaluation, Authorisation and Restriction of Chemicals (REACH) regulation defines a substance with a BCF higher than 2000 (or log BCF > 3.3) as bioaccumulative, while a substance with a BCF higher than 5000 (or log BCF > 3.7) is considered very bioaccumulative.

2.9.5. Biodegradability. The biodegradability of the test compounds was evaluated using the VEGA and ISIDA platforms. The IRFMN model provided by VEGA gives a qualitative prediction (readily biodegradable/not readily biodegradable), plus information about the reliability of the prediction (low, moderate, or high reliability). ISIDA provides a consensus regression model based on 15 individual models. The outcome

is given as a statement (readily biodegradable/not readily biodegradable) with a prediction confidence estimate (outside AD, average, good, and optimal).

2.9.6. Persistence. Persistence in sediment, soil, and water was evaluated using the VEGA and ISIGA platforms. Detailed information on the use of these models can be found in our previous work.[30] Briefly, the predictions from the different models were translated into a so-called persistence score that is a numeric value between 0 and 1, where 0 stands for not persistent and 1 stands for persistent. The classification for the graded translation for the VEGA models is given in Table S2,† while Table S3† shows the translation for ISIDA predictions.

Similar to the mutagenicity/carcinogenicity score, the arithmetic mean of the different generated prediction scores was calculated and interpreted as follows: a score higher than 0.66 means a positive prediction (persistent) with good reliability; a score lower than 0.33 means a negative prediction (not persistent) with good reliability; a score between 0.33 and 0.66 is considered equivocal. This includes the score range between 0.33 and 0.5, which is regarded a negative prediction (not persistent) with insufficient reliability, as well as the score range between 0.5 and 0.66, regarded a positive prediction (persistent) with insufficient reliability.

3. Results & discussions

3.1. Synthesis

Diethyl sinapoyl-L-malate (DESM) was prepared following the two-step procedure that Peyrot *et al.*[36] reported for the synthesis of SM. Nevertheless, for this Knoevenagel–Doebner condensation step, we decided to replace the hazardous pyridine/aniline couple with the eco-friendly ethanol/L-proline couple.[28] DESM was thus obtained from diethyl-L-malate and lignin-derived syringaldehyde, in two steps, with only one purification during the final step (Scheme 1).

Using the aforementioned procedure, di-*n*-butyl-sinapoyl-L-malate (DBSM) was prepared in 83% yield starting from di-*n*-butyl-L-malate, readily obtained from malic acid and ethanol using Fischer esterification. Unfortunately, this procedure proved unsuccessful for the synthesis of di-*n*-octyl-sinapoyl-L-malate (DOSM) as the Fischer esterification of malic acid with *n*-octanol was not quantitative, thus resulting in a mixture of several products for which flash chromatography purification

Scheme 1 Two-step synthesis of DESM.

Table 1 Optimized conditions for the transesterification of DESM into DOSM

DESM (eq.)	Octanol (eq.)	N435 (mg mmol^{-1})	T (°C)	Time (h)	P (mbar)	Isolated yield (%)
1	2.5	120	80	16	30	95

Scheme 2 Highly regioselective N435-catalyzed transesterification of DESM into the corresponding SM diesters.

Table 2 Yields of the transesterification of DESM with different alcohols

Alcohol	Compound	Yield (%)
Octanol	Dioctyl SM (DOSM)	95
Lauric alcohol (dodecanol)	Dilauryl SM (DLSM)	99
Citronellol	Dicitronellyl SM (DCSM)	97
Geraniol	Digeranyl SM (DGSM)	91
Farnesol	Difarnesyl SM (DFSM)	94
Oleic alcohol	Dioleylyl SM (DOleySM)	88

proved too complex as none of them absorb in the UV-Vis. It is noteworthy to mention that we faced the very same issue with alcohols carrying longer chains (*e.g.*, dodecanol, citronellol). Another strategy was thus needed to access DOSM, and other SM diester analogues, with minimal synthetic and purification steps. Still aiming at achieving the greenest process, we decided to study and optimize the biocatalyzed transesterification of DESM in the presence of supported *Candida antarctica* lipase B (also known as Novozym 435®, CALB or N435) for which high efficiency has been observed.[83–85] Indeed, in this strategy, the goal

was to take advantage of the low reactivity of N435 toward both the phenol moiety and the α,β-unsaturated ester, and determine whether it would result in a regioselective transesterification toward DESM that possesses two types of esters: the α,β-unsaturated ester that would remain untouched, and the two saturated esters from the malate moiety that would undergo transesterification without having to protect, and subsequently deprotect, the phenol moiety. To our delight, this strategy proved successful as the transesterification proceeds in almost total regioselectivity, exceeding all our expectations. This procedure was then optimized for the synthesis of DOSM (Table 1, Scheme 2) and subsequently implemented to the other desired sinapoyl malate diester with similar regioselectivity and yields (88–99%) (Table 2). It is worth mentioning that this synthetic procedure was successfully implemented at the kilo-scale.

3.2. UV-filtering properties and photostability

To explore the UV-filtering properties of the SM derivatives, UV analyses were carried out in ethanol (10^{-5} M, Fig. 2). In comparison with SM's UV spectrum ($\lambda_{max} = 332$ nm, Table 3), all SM derivatives showed very similar properties ($\lambda_{max} \approx 335$ nm,

Fig. 2 UV spectra of SM and SM diesters in EtOH.

Table 3 UV analysis: λ max, photostability and ε

Compounds	λ (nm)	Abs. loss (%)	ε (L mol^{-1} cm^{-1})
SM	332	25	20 814
DESM	334	26	20 482
DBSM	334	25	22 063
DOSM	335	27	23 045
DLSM	335	23	22 184
DCSM	336	18	19 776
DGSM	335	17	20 555
DFSM	336	16	21 254
DOleySM	336	15	19 091
Octinoxate™	310	27	24 046

Table 3), indicating that the additional fatty chains on the carboxylic acid functions do not disturb the UV-filtering potential of these new SM analogues.

Photostability is a key parameter for a UV-filter;[31] an efficient filtering compound should not lose its absorbance (at λ_{max}) during exposure to UVR. To assess photostability, we performed irradiation at 300 nm ($P = 8.32$ W m^{-2}) for one hour (t_{60}) at $T = 35$ °C and recorded the change in absorbance with UV spectroscopy. The UV spectrum after one hour of irradiation was then compared to the spectrum recorded before irradiation (t_0) and the loss in absorbance was measured at the λ_{max}. As an example, Fig. 3 highlights the photostability of DCSM, in which, post-UV irradiation, there is an 18% loss in absorbance at its λ_{max}. Photostability data in Table 3 were benchmarked against those of SM and Octinoxate™, the latter of which is a widely used and controversial UV-B filter contained in many sunscreen formulations.[86] SM had a loss of absorbance of 25% whilst DESM, DBSM, DOSM, and DLSM showed commensurate losses with 26, 25, 27, and 23% respectively. On the other hand, DCSM, DGSM, DFSM, and DOleySM exhibited smaller losses of 18, 17, 16 and 15%, respectively. It is noteworthy to mention that, under these specific photostability assay conditions, Octinoxate™ loss of absorbance was about 27%, as previously described.[28] Except for DOSM, all the new compounds exhibited better photostability than Octinoxate™ and could be

considered as interesting alternatives to this controversial compound for anti-UV applications.

Under UV exposure, photo-active α,β-unsaturated esters, such as the ones herein, are prone to form a cyclobutane ring (that does not exhibit any UV-filtering activity) with another neighbouring α,β-unsaturated ester through [2+2] photocyclization.[87] An efficient way to limit this photocyclization, and thus improve the photostability, is to increase the steric hindrance of the α,β-unsaturation.[28,31,33,34,88] Here, the introduction of aliphatic and non-ramified chains in DESM, DBSM, DOSM and DLSM, did not lead to better photostability (ca. 25% of absorbance loss, similar to that of SM), suggesting that the length of the additional group, even with C-8 and C-12 chains, is not enough to efficiently improve the steric hindrance, and therefore the photostability. Additionally, the introduction of citronellol and geraniol, both C-8 chains (DCSM and DGSM), bearing two methyl ramifications and double bond(s), led to an enhancement of the photostability (18% and 17% absorbance loss, respectively), highlighting the efficiency of the methyl ramifications and the double bond(s). This effect is confirmed with DFSM (C-12 chain, 3 methyl ramifications and 3 double bonds). The presence of these double bonds, leading to a folding back and not a linear part, promotes the intermolecular repulsions and therefore the photostability of the α,β-unsaturated moiety of the molecule (16% absorbance loss). Finally, DOleySM possesses the best photostability of the library with an absorbance loss of 15%. The two C-18 fatty chains, with a folding back due to the Z-configured C=C between the carbons 9 and 10, provide a very efficient shield to the sensitive α,β-unsaturated double bond. Compared to SM, the data demonstrate an enhanced photostability for the SM derivatives.

3.3. Antiradical activities

While direct protection against overexposure to UVR is crucial to ensure good development for crops, the use of multifunctional molecules can be a major asset by offering multiple properties and therefore, reducing the number of compounds used in a formulation. ROS are free radicals with high reactivity, produced by diverse metabolic pathways and involved in plant development.[89] ROS are also produced under stress conditions, such as excessive UVR exposure. An unregulated level of those free radicals can induce irreversible cellular damages (i.e., enzyme inactivation, membranes destruction) leading to cell death.[90] One way to prevent the negative impacts linked to high concentration of ROS is the presence of antiradical molecules, such as p-hydroxycinnamic derivatives, bearing a free phenol able to inhibit those radicals. In this regard, the antiradical properties of SM and its diester derivatives were assessed and benchmarked against references conventionally used, namely BHA (butylated hydroxyanisol) and BHT (butylated hydroxytoluene), by comparing their EC$_{50}$ (half-maximum effective concentration). EC$_{50}$ is defined as the amount (nmol) of antiradical compound needed to reduce half of DPPH free radicals; lower values correlate with higher antiradical properties. In addition, the kinetics of the radical scavenging was determined for each compound by using the EC$_{50}$ value to obtain the time

Fig. 3 UV photostability of DCSM.

Table 4 EC$_{50}$, $T_{EC_{50}}$ and kinetic behaviour of synthesized compounds for DPPH inhibition in ethanol

Compound	EC$_{50}$ (nmol)	$T_{EC_{50}}$ (s)	Kinetic
SM	8.5 ± 0.2	<60	Rapid
DESM	18.3 ± 0.4	<60	Rapid
DBSM	12.8 ± 0.3	<60	Rapid
DOSM	15.7 ± 0.9	<60	Rapid
DLSM	13.1 ± 0.3	<60	Rapid
DCSM	11.2 ± 0.1	<60	Rapid
DGSM	13.4 ± 0.2	<60	Rapid
DFSM	13.3 ± 0.3	<60	Rapid
DOleySM	14.3 ± 0.5	<60	Rapid
BHA	4.3 ± 0.1	380 ± 13	Intermediate
BHT	7.6 ± 0.2	>1800	Slow

needed to reach steady-state ($T_{EC_{50}}$) of radical inhibition. This parameter is used to sort antiradical properties in three behaviours: slow ($T_{EC_{50}} > 1800$ s), intermediate ($300 < T_{EC_{50}} < 1800$ s) and rapid ($T_{EC_{50}} < 300$ s) as previously described by Sánchez-Moreno et al.[91] The results are summarized in Table 4. The introduction of ester moieties in place of the two free carboxylic acids proved to have a negative impact as, from a general point of view, all diester derivatives exhibited lower antiradical activity (i.e., higher EC$_{50}$) than the base SM. Focussing only on the analogues, the nature of the ester moiety had little impact on the activity towards free radicals – which is in accordance with a previous study on p-hydroxycinnamic

derivatives[32] – as EC$_{50}$ values were in the same range (11.2–15.7 nmol), with the exception of DESM (18.3 nmol). Regarding their kinetics, all compounds reached a steady-state of radical inhibition under 60 s, exhibiting rapid activity, which was significantly better than BHA and BHT references. Despite exhibiting higher EC$_{50}$ values than both references, SM diester derivatives make viable antiradicals with dual activity by combining swift inhibition of free radicals and UV filter properties.

3.4. Transient absorption spectroscopy

The transient electronic absorption (TEA) spectra obtained for SM and its derivatives following photoexcitation at their respective UV absorption λ_{max} in caprylic capric triglyceride are reported in Fig. 4. The observed TEA spectra are similar in all cases, each having three spectral features. First is the negative feature at the blue edge of the probe window (∼350 nm) of the TEA spectra; we assign this feature to the ground state bleach (GSB) through comparison with the steady-state UV/visible spectra (see Fig. 2) and previously reported works on SM.[12,16] Second is an intense positive feature centered at ∼430 nm which we attribute to the excited-state absorption (ESA) in line with the literature. Lastly, on closer inspection, there is a broad and weaker ESA feature that begins at ∼470 nm and extends to the end of our probe window (700 nm). While all the aforementioned spectral features seem to have decayed to baseline within pump-probe delay time of 100 picoseconds (ps) through visual inspection, the 2 ns transient data presented in ESI

Fig. 4 TEA spectra in caprylic capric triglyceride bulk solution for (A) SM, (B) DESM, (C) DBSM (D) DOSM, (E) DLSM, (F) DCSM, (G) DGSM, (H) DFSM, and (I) DOleySM in the form of a false colour heat map indicating change in optical density (ΔOD). In all cases, the delay time is presented on a linear plot until 1 ps and then as a logarithmic scale between 1 ps and 2 ns.

Table 5 Summary of the time constants and associated errors extracted from fitting TEA spectra for SM and its derivatives in the bulk solution of caprylic capric triglyceride

Compounds	τ_1 (fs)	τ_2 (fs)	τ_3 (ps)	τ_4 (ns)
SM	100 ± 60	550 ± 60	20.1 ± 0.2	>2
DESM	120 ± 60	970 ± 60	19.3 ± 0.1	>2
DBSM	110 ± 60	950 ± 60	19.8 ± 0.1	>2
DOSM	100 ± 60	830 ± 60	20.0 ± 0.2	>2
DLSM	110 ± 60	930 ± 60	21.7 ± 0.2	>2
DCSM	100 ± 60	850 ± 60	21.3 ± 0.2	>2
DGSM	110 ± 60	1070 ± 60	21.8 ± 0.2	>2
DFSM	110 ± 60	1040 ± 60	22.8 ± 0.1	>2
DOleySM	130 ± 60	1260 ± 60	23.8 ± 0.1	>2

Fig. S45† revealed that a residual GSB and ESA at ~430 nm persists. We return to discuss the implication of this persistent feature on the dynamics and suitability of SM derivatives in molecular heater applications.

To gain insight into the dynamical process and extract the excited state kinetic information from the presented TEA spectra of each molecule, a global sequential fitting procedure $(A \xrightarrow{\tau_1} B \xrightarrow{\tau_2} C \xrightarrow{\tau_3} D\ldots)$ implemented through the Glotaran software package was employed. The extracted time constants and associated errors returned by the fitting software to twice the standard errors are reported in Table 5. The evolution associated difference spectra (EADS) for each fit are also shown in the ESI Fig. S46.† The quality of the fits is better evaluated by inspecting the associated residuals from the fit, reported in Fig. S47.† Where the returned standard error was shorter than the instruments response time, the error is quoted as half of the instrument response (as determined through the solvent-only scan presented in Fig. S48†).

We now assign dynamical processes to the extracted time constants reported in Table 5, and discuss their implications drawing on previous studies on SM.[12,92–95] The similarity between the information extracted from SM and its derivatives in the current work is an indication that the relaxation mechanism likely remains largely unchanged upon the addition of a long chain fatty acid. Hence, we assign the dynamical processes to the extracted time constants as a collective. The first dynamical process defined by τ_1 occurs on a time-constant between 100 and 130 femtoseconds (fs) in all the molecules. Previous work on SM and its derivatives has assigned a number of mechanisms to this initial process following photoexcitation to the $1^1\pi\pi^*$ state, this includes rapid geometry and vibrational relaxation out of the Franck–Condon region and solvent rearrangement. We, therefore, attribute τ_1 to the aforementioned dynamical processes. It is worth noting that τ_1 for SM returned a short time constant of 70 fs which is within the IRF, however this time component is needed for the accurate fitting of the data.

Two different mechanisms have been previously assigned to the dynamical process associated with the time constant denoted τ_2.[12] The first is the internal conversion (IC) of the $1^1\pi\pi^*$ state to the $2^1\pi\pi^*$ state through $1^1\pi\pi^*/2^1\pi\pi^*$ conical intersection (CI). The second is the evolution of the S_1 population along the potential energy surface towards the $1^1\pi\pi^*/S_0$

CI. Recent computational studies favour the latter mechanism; the $1^1\pi\pi^*/2^1\pi\pi^*$ CI is either absent or inaccessible.[96] Hence, we suggest that τ_2 extracted from our study corresponds to the evolution of the $1^1\pi\pi^*$ population towards the S_1/S_0 CI. The dynamical process associated with τ_3 is attributed to the $1^1\pi\pi^*$ population traversing the S_1/S_0 CI to the ground state along the trans–cis isomerization coordinate along with subsequent vibrational cooling. This dynamical process results in a fraction of the excited state population returning to the ground state in the form of the starting trans-isomer. The second fraction completes the isomerization along the C=C allylic bond twist to generate the cis-isomer as a photoproduct. Although, the EADS (see Fig. S45†) and the resulting time constants from our fitting model suggests that the ground state formation of the starting trans-isomer and cis-isomer product following relaxation from the excited state are achieved in a single process (EADS$_3$, τ_3), there is the possibility that both the processes occur on different timescales that are not separable by our experimental method. Indeed, previous time-resolved vibrational spectroscopy on ethyl sinapate, a derivative of sinapoyl malate, revealed that the relaxation of the starting trans-isomer is achieved on a faster time constant of ~10 ps compared to the cis-isomer product with a time constant of ~20 ps in the ground electronic state.[97] The signature of the cis-isomer photoproduct is evident in EADS$_4$ (Fig. S45†) with a positive absorption band at ~370 nm and having a time-constant greater than 2 ns.[12] Assignment of EADS$_4$, to the cis-isomer photoproduct, is supported through a comparison of the $\Delta t = 2$ ns transient absorption profile shown in Fig. S45† to those reported for SM and its derivatives previously, which show an identical feature in the spectral region of interest.[12]

In summary, the dynamical process reported for SM and its derivatives implies that the absorbed light by the UV filters is efficiently dissipated non-radiatively as heat to the surrounding solvent bath, strongly suggesting that SM derivatives are suitable for application as a molecular heater.

3.5. LC-MS-IRIS study

3.5.1. LC-MS-IRIS study on solar degradation product of DOSM. DOSM was degraded by simulated solar irradiation, and LC-MS was employed to characterize the degradation products. We identify features that are unique to the degraded sample of DOSM (Fig. 5) compared to the non-irradiated DOSM sample. Fig. 5A depicts the base-peak chromatograms (BPCs) of both DOSM samples, showing two features that increase in intensity after irradiation.

The first feature elutes at 13.35 min at an m/z of 587; the same m/z is observed in the non-irradiated DOSM but at a retention time (RT) of 13.25 min as a baseline-separated feature. Additionally, we note that both features' MS/MS fragmentation patterns are identical. In the non-degraded DOSM sample, this m/z is attributed to the sodium adduct of DOSM. As DOSM is synthesized as a pure trans-isomer and we know that the modus operandi of the photomolecular heater is based on isomerization reactions, we attribute the newly generated feature to the cis-isomerized form of DOSM.

Fig. 5 Feature of interest characterization of a DOSM degradation product compared with DO2HS synthesized reference. (A) BPC chromatograms of samples, where non-degraded DOSM is plotted in blue, degraded DOSM in black, and the DO2HS standard in green. (B) MS/MS fragmentation pattern of DOSM degradation product at m/z 359 in black and the DO2HS standard in green, where orange indicates the m/z 359 precursor. (C) MS/MS fragmentation pattern of DOSM degradation product at m/z 381 in black and the DO2HS standard in green, where orange indicates the m/z 381 precursor. (D) IR ion spectrum of DOSM degradation product at m/z 359 in black and the protonated DO2HS standard in green. The green-filled curve represents the DFT predicted IR spectrum with absorption lines discussed in the text as vertical black bars. (E) IR ion spectrum of DOSM degradation product at m/z 381 in black and the protonated DO2HS standard in green. The green-filled curve represents the DFT predicted IR spectrum with absorption bands discussed in the ESI† as vertical black bars.

A second feature is observed at 13.12 minutes with an m/z of 381, which is assumed to be a sodium adduct since the protonated feature at m/z 359 is also observed, but not as the base peak in the chromatogram. Considering the molecular structure of DOSM, the observed m/z value could correspond to the fragment remaining after cleaving off the ester group from the sinapoyl moiety, leaving it as an aldehyde. The complementary fragment is presumably di-octyl-2-hydroxy succinate (DO2HS), as depicted in Scheme 3. CID fragmentation of the m/z 381 ion yields a primary product at m/z 269, which can then be rationalized as expulsing one of the octyl groups. We do not observe the complementary DOSM degradation product, indicated as SAL in Scheme 3. This fragment could be obscured by in-source fragmentation forming an acylium ion (SALOX) that is observed as an ion at m/z 207, which is seen for all peaks containing the sinapoyl moiety.[98–100] Alternatively, the highly reactive oxonium ion formation may explain the absence of SAL in

the chromatographic analysis. Some additional degradation products at significantly lower abundances are observed, which we shall not further discuss here.

Chromatograms, MS/MS, and IRIS spectra for both the photoproduct and the synthesized DO2HS reference standard are plotted in Fig. 5. The positive y-axis represents the photoproduct, while the negative axis represents the reference standard. Fig. 5D and E show the IRIS spectra for both the protonated and sodiated species. The IR photodissociation yield spectrum (eqn (1)) is shown for the protonated species. No characteristic fragments were observed for the sodiated species, unlike in CID. This suggests that the sodium ion is detached during IRMPD but remains undetected since m/z 23 is below the low-mass cut-off of the QIT.[74] The depletion spectrum obtained using eqn (2) is slightly noisier. We observe a reasonable match for both spectra with the IR spectrum of DO2HS predicted by density functional theory (DFT) for the protonated and sodiated species. Therefore,
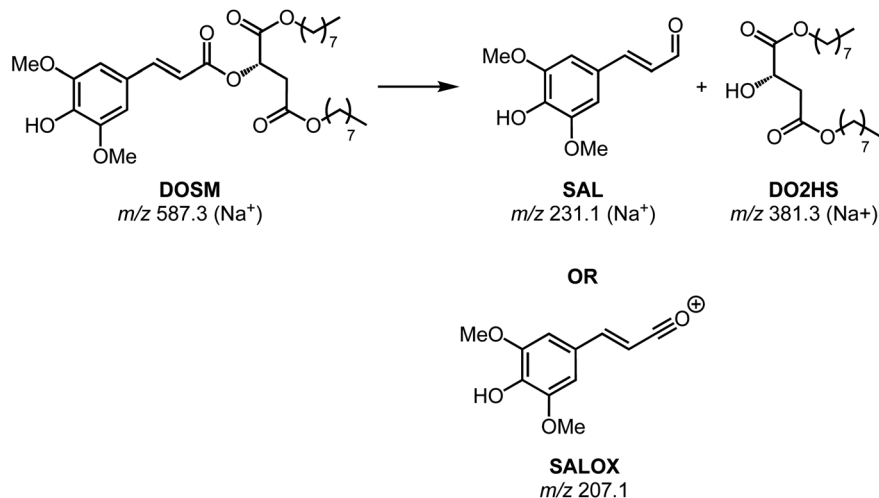
Scheme 3 Proposed degradation product formation of DOSM. The suggested degradation reaction results in the ester cleavage of DOSM into a sinapoyl aldehyde fragment (SAL) and an alcoholic di-octyl-2-hydroxy succinate (DO2HS).

we tentatively assign the DO2HS structure to the detected degradation product; a reference DO2HS standard was then synthesized in-house to evaluate whether the UV-photoproduct indeed corresponds to the suggested DO2HS candidate.

The chromatographic analysis in Fig. 5A indicates that DO2HS retention matches the feature found in the degradation sample. The MS/MS fragmentation pattern for both the protonated and sodiated adducts, shown in Fig. 5B and C, are identical for the DO2HS reference standard and the degradation feature, providing a confident LC-MS/MS match. The tentative structure assignment based on IRIS facilitated a targeted comparison with the reference standard. We can also match the IRIS spectra for the degradation product and the synthesized DO2HS reference; see Fig. 5D and E. All spectral features match peak position and relative intensity, confirming our structural identification. Based on the DFT match, absorption bands in the IRIS spectrum can be assigned to specific vibrational normal modes, as indicated with vertical sticks and discussed in more detail in the ESI.†

3.5.2. LC-MS-IRIS study on solar degradation of DGSM. Similarly to DOSM, DGSM was degraded through simulated solar irradiation inside a quartz-topped cuvette. Furthermore, during field trials of this compound, leaf extracts were obtained and analyzed by LC-MS to evaluate the formation of degradation products. The BPC analysis of a sample combining extracts of four replicate field trial experiments is presented in Fig. 6.

Chromatographic features of interest are identified by comparing degraded and non-degraded DGSM. DGSM elutes at 16.00 min at m/z of 635 as the sodiated ion. After degradation, similar to what was observed in DOSM, we found an isomeric feature at 16.05 min, which is attributed to the *cis*-isomerized product of DGSM. More interestingly, we observe an additional feature at 15.75 min with an m/z of 429, which was also encountered in the field trial extracts, indicating that the feature is formed *in vitro* and *in vivo*. The accurate mass value of the m/z 429 ion suggests an ester cleavage product similar to DO2HS. The alcoholic di-geraniol-2-hydroxy succinate (DG2HS)

that is hypothesized to form in this case is depicted in Scheme 4. We investigated this ion further using IRIS spectroscopy, as shown in Fig. 6.

Fig. 6C depicts the IRIS spectrum of the Cs$^+$-adduct of DG2HS along with a DFT-predicted IR spectrum. The cesium ion adduct gave a better quality spectrum than the Na$^+$ adduct (recorded in depletion; see above for the DO2HS). As compared to Na$^+$, the weaker binding energy of Cs$^+$ often generates cleaner IRMPD spectra, where the cesium ion acts as a weakly-bound messenger tag,[101–105] and moreover, Cs$^+$ is easier to detect in the QIT-MS due to its higher mass. The match between the experimental and theoretical spectra is sufficiently convincing for a tentative assignment based on the features above 1000 cm^{-1}, and warranted the synthesis of a reference standard of DG2HS.

The top part of Fig. 6A shows the chromatograms of the photoproduct from the solar simulation and field trial extract, with the reference standards results displayed as an inverted curve. Fig. 6B depicts the MS/MS spectrum of the field trial extract at m/z 429 and the reference standard in the inverted axes. This figure shows that the feature of interest and the DG2HS reference standard have the same retention time and MS/MS fragmentation pattern, which strongly suggests that they are the same molecule. In addition, we compared the IR ion spectrum of the photoproduct in the solar simulation, the field trial extract, and the DG2HS reference standard – also synthesized in-house – presented in Fig. 6C. This comparison confirms the assignment and enables us to confidently associate specific vibrational modes with the observed spectral characteristics, as further detailed in the ESI.†

3.6. *In silico* predictions

3.6.1. Mutagenicity/carcinogenicity/endocrine toxicity. As shown in Fig. 7, all mutagenicity scores were around or below 0.33, indicating that the test compounds and the degradation products of DOSM are predicted to be non-mutagenic. Carcinogenicity scores mostly ranged between the thresholds 0.5 and 0.33. Thus, the test compounds are predicted to be non-

Fig. 6 Feature of interest characterizing a DGSM degradation product compared with DG2HS synthesized reference. (A) BPC chromatograms of samples, where non-degraded DGSM is plotted in blue, degraded DGSM in black, field trial extract EU08 (cucumber DGSM (BC-05-16 2.5 L ha^{-1})) in dark green, and the DG2HS standard in green (inverted). (B) MS/MS fragmentation pattern of DGSM degradation product at m/z 429 in black and the DG2HS standard in green, where orange indicates the m/z 429 precursor. (C) IR ion spectrum of DGSM degradation product at m/z 539 in black, field trial extract EU08 (cucumber DGSM (BC-05-16 2.5 L ha^{-1})) in dark green, and the cesium ion DG2HS standard in green (inverted). The green-filled curve represents the DFT-predicted IR spectrum with absorption bands discussed in the ESI† as vertical black bars.

carcinogenic, but the reliability of the predictions is not optimal.

Regarding endocrine toxicity, all test compounds were predicted to have binding affinity for the estrogen receptor, but the reliability was low (Table S4†). Besides, all of them were predicted inactive with regards to estrogen receptor-mediated effects (all predictions with good reliability except for DGSM

being of moderate reliability). Moreover, they were all predicted inactive with regards to the androgen receptor, with moderate reliability. None of the test compounds were predicted to exert effects *via* thyroid receptors (all predictions with good reliability). In regards to the DOSM degradation products, DO2HS was predicted to have binding affinity for the estrogen receptor (with low reliability) but was predicted inactive with good

Scheme 4 Schematic of proposed degradation product formation of DGSM.

Fig. 7 Schematic presentation of the results of the *in silico* analysis with regard to the endpoint mutagenicity, and carcinogenicity. The test compounds are listed by their average prediction score on the *y* axis. In addition, the prediction scores were divided in three different groups (dashed lines): the probable mutagens/carcinogens with scores greater than 0.66, the probably non-mutagens/non-carcinogens with scores smaller than 0.33, and the remaining equivocal predictions with scores between 0.33 and 0.66.
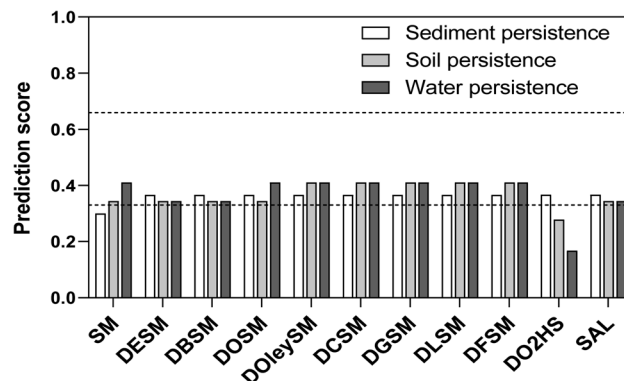
Fig. 8 Schematic presentation of the results of the *in silico* analysis with regard to the endpoint persistence (sediment, soil, and water). The test compounds are shown with their average prediction score. In addition, the prediction scores were divided in three different groups (dashed lines): the probable persistent substances with scores greater than 0.66, the probably non-persistent substances with scores smaller than 0.33, and the remaining equivocal predictions with scores between 0.33 and 0.66.

reliability for all other receptors. SAL was predicted to be active towards androgen receptor with low reliability while inactive towards all other receptors (with good or low reliability).

3.6.2. Acute and repeated-dose toxicity. Oral LD_{50} and NOAEL in rats were used as representative endpoints for acute and repeated-dose toxicity (90 day study). The estimated values for LD_{50} were between 580 and 14 600 mg kg^{-1} body weight (bw) (Table S5†). The estimated NOAELs ranged between 60 and 1050 mg kg^{-1} bw per day.

3.6.3. Bioaccumulation. All test compounds showed a log BCF < 3.3 (with good reliability for ISIDA, see Table S6†), indicating that they are not predicted to be bioaccumulative. Similar outcome was observed for the DOSM degradation products.

3.6.4. Biodegradability. All test compounds were predicted to be readily biodegradable according to VEGA (all with moderate reliability, except DGSM), while ISIDA predicted all compounds to be not readily biodegradable (mostly with good prediction confidence, see Table S7†). Therefore, a firm conclusion cannot be drawn regarding the biodegradability of the test compounds. However, it is noteworthy that the DOSM degradation products were predicted to be readily biodegradable by both models with moderate or good reliability.

3.6.5. Persistence. Overall, sediment persistence scores were very close to the threshold of 0.33. Thus, it is expected that the test compounds and the DOSM degradation products are not persistent in sediment. Soil and water persistence scores were below 0.5, but above the threshold of 0.33. This indicates that the test compounds are predicted to be non-persistent in soil and water, but the reliability of the predictions is not optimal (Fig. 8). It is noteworthy that scores for DESM, DBSM, and SAL are very close to 0.33, thus the reliability in their non-persistence in soil and water is higher than for the other compounds. Soil and water persistence scores for DO2HS were

below the threshold of 0.33, indicating that this byproduct is not predicted to be persistent in those compartments.

In summary, we used a battery of different *in silico* models to gain information on both toxicity and environmental aspects. The outcomes of the different predictions did not show a critical potential for toxicity (especially mutagenicity) or environmental persistence. Thus, in view of the preliminary *in silico* data, no particular alert prohibits from further development of the test compounds regarding their use as molecular heaters. However, it is important to stress out that *in silico* approaches do not replace *in vitro* and/or *in vivo* toxicological testing. For admission of the test compounds to the market, a wide toxicological examination will be required to constitute a proper submission dossier. Such examination is, nonetheless, beyond the scope of this study.

4. Conclusions

Herein, we have reported a high-yielding (88–99%) and highly selective green biocatalytic pathway to bio-based fatty chains-bearing SM derivatives. These latest molecules exhibit similar UV-filtering properties to SM ($\lambda_{max} \approx 335$ nm), indicating that the additional fatty chains do not disrupt the UV-filtering potential of these new analogues. Their photostability showed that, with the omission of DOSM (27%), all the new analogues exhibited better photostability (*i.e.*, loss of absorbance) than Octinoxate™ (15–26% *vs.* 27%). It is noteworthy to mention that analogues bearing unsaturated fatty chains (DCSM, DGSM, DFSM and DOleySM) exhibited the strongest photostabilities (15–18%). These compounds might thus be considered as a valuable bio-based alternative to the controversial and petroleum based commercial UV filters. Conversely, the addition of ester moieties in place of the two free carboxylic acids proved to have a negative impact on the antioxidant activity. Although all SM derivatives exhibited higher EC_{50} (11.2–18.3 nmol) than SM

(8.5 nmol), these antioxidant activities still remain interesting for five compounds (DBSM, DLSM, DCSM, DGSM and DFSM, EC$_{50}$: 11.2–13.4 nmol).

The photophysics of these SM derivatives following absorption of UV radiation has also been studied through ultrafast transient absorption spectroscopy. The results showed that the relaxation mechanism in these molecules is the same as that of SM, returning to the ground state on an ultrafast time scale. The relaxation mechanism has been determined to be initiated by geometry relaxation out of the Franck–Condon region, followed by S$_1$/S$_0$ internal conversion resulting in the formation of both starting *trans* isomer and *cis* isomer photoproduct. This relaxation process results in the dissipation of the absorbed energy to the solvent environment as vibrational energy (*i.e.*, heat), thereby making these SM derivatives suitable for application where efficient light-to-heat conversion is required.

In order to evaluate the toxicological properties of the test compounds, we ran a battery of *in silico* analyses to cover key endpoints such as mutagenicity, carcinogenicity, or oral acute toxicity. Environmental aspects (*e.g.*, bioaccumulation, persistence) were also covered. No critical potential for toxicity (especially mutagenicity) or environmental persistence were noticed for the test compounds and analysis for the two degradation products of DOSM also showed no alerts. These *in silico* predictions should be confirmed by adequate *in vitro* and/or *in vivo* testing as computational modelling is not yet able to replace classical testing methodologies.

Considering their green synthesis, UV filtering activity, photostability, photophysics, lack of critical toxicity, lack of persistence and bioaccumulation and ability to interact with waxy cuticle of plants, and to be readily incorporated in cosmetic formulations, the SM derivatives studied in this work are promising for application as UV filters in cosmetics, as well as molecular heaters in crop protection through incorporation in a foliar spray.

Data availability

The data that support the findings of this study are available upon request.

Author contributions

F. A., V. G. S., A. B., and J. O. conceived the original research and acquired funding. B. R., L. M. M. M., M. M. M., A. A. M. P. and F. B. performed the synthesis, characterizations, UV and photostabilities analysis, and antiradical analysis. T. T. A. acquired and analyzed the transient absorption data. T. T. A. acquired and analyzed the steady-state spectroscopy data with assistance from J. M. W. J. A. conducted and analyzed the *in silico* toxicology studies. M. J. A. V. performed the LC-MS-IRIS study on the solar degradation product of DOSM. G. B. and J. O. contributed in the interpretation and analysis of the LC-MS-IRIS study. B. R., L. M. M. M., M. M. M., T. T. A., M. J. A. V., J. M. W. and J. A. contributed to writing the manuscript. F. A., A. B., G. B., J. O. and V. G. S. reviewed and corrected the manuscript.

Conflicts of interest

There are no conflicts to declare.

Acknowledgements

References

1 H. Jin, E. Cominelli, P. Bailey, A. Parr, F. Mehrtens, J. Jones, C. Tonelli, B. Weisshaar and C. Martin, *EMBO J.*, 2000, **19**, 6150–6161, DOI: **10.1093/emboj/19.22.6150**.

2 L. A. Baker, B. Marchetti, T. N. V. Karsili, V. G. Stavros and M. N. R. Ashfold, *Chem. Soc. Rev.*, 2017, **46**, 3770–3791, DOI: **10.1039/C7CS00102A**.

3 C. Barta, T. Kálai, K. Hideg, I. Vass and É. Hideg, *Funct. Plant Biol.*, 2004, **31**, 23–28, DOI: **10.1071/FP03170**.

4 G. I. Jenkins, *Annu. Rev. Plant Biol.*, 2009, **60**, 407–431, DOI: **10.1146/annurev.arplant.59.032607.092953**.

5 H. Frohnmeyer and D. Staiger, *Plant Physiol.*, 2003, **133**, 1420–1428, DOI: **10.1104/pp.103.030049**.

6 A. Glasauer and N. S. Chandel, *Curr. Biol.*, 2013, **23**, R100–R102, DOI: **10.1016/j.cub.2012.12.011**.

7 A. Glasauer and N. S. Chandel, *Biochem. Pharmacol.*, 2014, **92**, 90–101, DOI: **10.1016/j.bcp.2014.07.017**.

8 R. Mittler, *Trends Plant Sci.*, 2017, **22**, 11–19, DOI: **10.1016/j.tplants.2016.08.002**.

9 J. Li, T. M. Ou-Lee, R. Raba, R. G. Amundson and R. L. Last, *Plant Cell*, 1993, **5**, 171–179, DOI: **10.1105/tpc.5.2.171**.

10 V. Yadav, Z. Wang, C. Wei, A. Amo, B. Ahmed, X. Yang and X. Zhang, *Pathogens*, 2020, **9**, 312, DOI: **10.3390/pathogens9040312**.

11 A. Sharma, B. Shahzad, A. Rehman, R. Bhardwaj, M. Landi and B. Zheng, *Molecules*, 2019, **24**, 2452, DOI: **10.3390/molecules24132452**.

12 L. A. Baker, M. D. Horbury, S. E. Greenough, F. Allais, P. S. Walsh, S. Habershon and V. G. Stavros, *J. Phys.*

Chem. Lett., 2016, **7**, 56–61, DOI: **10.1021/acs.jpclett.5b02474**.

13 C. M. Fraser and C. Chapple, *Arabidopsis*, 2011, **9**, e0152, DOI: **10.1199/tab.0152**.

14 R. A. Dixon, L. Achnine, P. Kota, C.-J. Liu, M. S. S. Reddy and L. Wang, *Mol. Plant Pathol.*, 2002, **3**, 371–390, DOI: **10.1046/j.1364-3703.2002.00131.x**.

15 L. A. Baker and V. G. Stavros, *Sci. Prog.*, 2016, **99**, 282–311, DOI: **10.3184/03685016X14684992086383**.

16 M. D. Horbury, W. D. Quan, A. L. Flourat, F. Allais and V. G. Stavros, *Phys. Chem. Chem. Phys.*, 2017, **19**, 21127–21131, DOI: **10.1039/C7CP04070A**.

17 K. Osakabe and Y. Osakabe, *eLS*, 2012, DOI: **10.1002/9780470015902.a0001319.pub2**.

18 T. T. Abiola, B. Rioux, J. M. Toldo, J. Alarcan, J. M. Woolley, M. A. P. Turner, D. J. L. Coxon, M. Telles do Casal, C. Peyrot, M. M. Mention, W. J. Buma, M. N. R. Ashfold, A. Braeuning, M. Barbatti, V. G. Stavros and F. Allais, *Chem. Sci.*, 2021, **12**, 15239–15252, DOI: **10.1039/D1SC05077J**.

19 A. Jesus, E. Sousa, M. T. Cruz, H. Cidade, J. M. S. Lobo and I. F. Almeida, *Pharmaceuticals*, 2022, **15**, 263, DOI: **10.3390/ph15030263**.

20 L. Ouchene, I. V. Litvinov and E. Netchiporouk, *J. Cutaneous Med. Surg.*, 2019, **23**, 648–649, DOI: **10.1177/1203475419871592**.

21 S. Suh, C. Pham, J. Smith and N. A. Mesinkovska, *Int. J. Dermatol.*, 2020, **59**, 1033–1042, DOI: **10.1111/ijd.14824**.

22 K. U. Schallreuter, J. M. Wood, D. W. Farwell, J. Moore and H. G. M. Edwards, *J. Invest. Dermatol.*, 1996, **106**, 583–586, DOI: **10.1111/1523-1747.ep12344991**.

23 R. D. Kouchi, *A Bill for an Act Relating to Water Pollution*, **https://www.capitol.hawaii.gov/Archives/measure_indiv_Archives.aspx?billnumber=132&billtype=SB&year=2021**, accessed February 23rd 2022.

24 D. Vuckovic, I. Tinoco Amanda, L. Ling, C. Renicke, R. Pringle John and A. Mitch William, *Science*, 2022, **376**, 644–648, DOI: **10.1126/science.abn2600**.

25 P. Anastas and J. Warner, *Green Chemistry: Theory and Practice*, Oxford Univ Press, 1998.

26 W. Setyaningsih, I. E. Saputro, C. A. Carrera and M. Palma, *Food Chem.*, 2019, **288**, 221–227, DOI: **10.1016/j.foodchem.2019.02.107**.

27 D. Rais and S. Zibek, *Adv. Biochem. Eng./Biotechnol.*, 2019, **166**, 469–518, DOI: **10.1007/10_2017_6**.

28 B. Rioux, C. Peyrot, M. M. Mention, F. Brunissen and F. Allais, *Antioxidants*, 2020, **9**, 331, DOI: **10.3390/antiox9040331**.

29 L. M. M. Mouterde, A. A. M. Peru, M. M. Mention, F. Brunissen and F. Allais, *J. Agric. Food Chem.*, 2020, **68**, 6998–7004, DOI: **10.1021/acs.jafc.0c02183**.

30 B. Rioux, M. M. Mention, J. Alarcan, T. T. Abiola, C. Peyrot, F. Brunissen, A. Braeuning, V. G. Stavros and F. Allais, *Green Chem. Lett. Rev.*, 2022, **15**, 114–125, DOI: **10.1080/17518253.2021.2022219**.

31 M. D. Horbury, E. L. Holt, L. M. M. Mouterde, P. Balaguer, J. Cebrian, L. Blasco, F. Allais and V. G. Stavros, *Nat. Commun.*, 2019, **10**, 1–8, DOI: **10.1038/s41467-019-12719-z**.

32 C. Peyrot, M. M. Mention, F. Brunissen and F. Allais, *Antioxidants*, 2020, **9**, 782, DOI: **10.3390/antiox9090782**.

33 C. Peyrot, M. M. Mention, F. Brunissen, P. Balaguer and F. Allais, *Molecules*, 2020, **25**, 2178, DOI: **10.3390/molecules25092178**.

34 M. M. Mention, A. L. Flourat, C. Peyrot and F. Allais, *Green Chem.*, 2020, **22**, 2077–2085, DOI: **10.1039/d0gc00122h**.

35 T. T. Abiola, N. d. N. Rodrigues, C. Ho, D. J. L. Coxon, M. D. Horbury, J. M. Toldo, M. T. do Casal, B. Rioux, C. Peyrot, M. M. Mention, P. Balaguer, M. Barbatti, F. Allais and V. G. Stavros, *J. Phys. Chem. Lett.*, 2021, **12**, 337–344, DOI: **10.1021/acs.jpclett.0c03004**.

36 C. Peyrot, M. M. Mention, R. Fournier, F. Brunissen, J. Couvreur, P. Balaguer and F. Allais, *Green Chem.*, 2020, **22**, 6510–6518, DOI: **10.1039/D0GC02763D**.

37 J. Ashraf, E. U. Mughal, A. Sadiq, M. Bibi, N. Naeem, A. Ali, A. Massadaq, N. Fatima, A. Javid, M. N. Zafar, B. A. Khan, M. F. Nazar, A. Mumtaz, M. N. Tahir and M. Mirzaei, *J. Biomol. Struct. Dyn.*, 2021, **39**, 7107–7122, DOI: **10.1080/07391102.2020.1805364**.

38 M. Balakrishna, S. S. Kaki, M. S. L. Karuna, S. Sarada, C. G. Kumar and R. B. N. Prasad, *Food Chem.*, 2017, **221**, 664–672, DOI: **10.1016/j.foodchem.2016.11.121**.

39 B. Rioux, A. Pinon, A. Gamond, F. Martin, A. Laurent, Y. Champavier, C. Barette, B. Liagre, C. Fagnère, V. Sol and C. Pouget, *Eur. J. Med. Chem.*, 2021, **222**, 113586, DOI: **10.1016/j.ejmech.2021.113586**.

40 B. Rioux, C. Pouget, C. Fidanzi-Dugas, A. Gamond, A. Laurent, J. Semaan, A. Pinon, Y. Champavier, D. Y. Leger, B. Liagre, J.-L. Duroux, C. Fagnere and V. Sol, *Bioorg. Med. Chem. Lett.*, 2017, **27**, 4354–4357, DOI: **10.1016/j.bmcl.2017.08.024**.

41 B. Rioux, C. Pouget, G. M. A. Ndong-Ntoutoume, R. Granet, A. Gamond, A. Laurent, A. Pinon, Y. Champavier, B. Liagre, C. Fagnere and V. Sol, *Bioorg. Med. Chem. Lett.*, 2019, **29**, 1895–1898, DOI: **10.1016/j.bmcl.2019.05.056**.

42 G. Seelinger, I. Merfort and C. M. Schempp, *Planta Med.*, 2008, **74**, 1667–1677, DOI: **10.1055/s-0028-1088314**.

43 M. Funakoshi-Tago, K. Nakamura, K. Tago, T. Mashino and T. Kasahara, *Int. Immunopharmacol.*, 2011, **11**, 1150–1159, DOI: **10.1016/j.intimp.2011.03.012**.

44 R. Ginwala, R. Bhavsar, D. G. I. Chigbu, P. Jain and Z. K. Khan, *Antioxidants*, 2019, **8**, 35, DOI: **10.3390/antiox8020035**.

45 W. Fan, S. Qian, P. Qian and X. Li, *Virus Res.*, 2016, **220**, 112–116, DOI: **10.1016/j.virusres.2016.04.021**.

46 S. L. Badshah, S. Faisal, A. Muhammad, B. G. Poulson, A. H. Emwas and M. Jaremko, *Biomed. Pharmacother.*, 2021, **140**, 111596, DOI: **10.1016/j.biopha.2021.111596**.

47 A. Di Petrillo, G. Orrù, A. Fais and M. C. Fantini, *Phytother. Res.*, 2022, **36**, 266–278, DOI: **10.1002/ptr.7309**.

48 L. Minsat, C. Peyrot, F. Brunissen, J.-H. Renault and F. Allais, *Antioxidants*, 2021, **10**, 512, DOI: **10.3390/antiox10040512**.

49 J. Liu, C. Chen, F. Wu and L. Zhao, *Chem. Biol. Drug Des.*, 2013, **82**, 39–47, DOI: **10.1111/cbdd.12126**.

50 S. Y. Lee, N. Baek and T.-g. Nam, *J. Enzyme Inhib. Med. Chem.*, 2016, **31**, 1–13, DOI: **10.3109/14756366.2015.1004058**.

51 E. Knoevenagel, *Ber. Dtsch. Chem. Ges.*, 1894, **27**, 2345–2346, DOI: **10.1002/cber.189402702229**.

52 L. M. M. Mouterde and F. Allais, *Front. Chem.*, 2018, **6**, 426, DOI: **10.3389/fchem.2018.00426**.

53 P. Singh and M. Kaur, *Chem. Commun.*, 2011, **47**, 9122–9124, DOI: **10.1039/C1CC12668G**.

54 J. K. Rajput and G. Kaur, *Chin. J. Catal.*, 2013, **34**, 1697–1704, DOI: **10.1016/S1872-2067(12)60646-9**.

55 X. Hu, C. Ngwa and Q. Zheng, *Curr. Org. Synth.*, 2016, **13**, 101–110, DOI: **10.2174/1570179412666150505185134**.

56 D. C. Forbes, A. M. Law and D. W. Morrison, *Tetrahedron Lett.*, 2006, **47**, 1699–1703, DOI: **10.1016/j.tetlet.2006.01.059**.

57 K. Isobe, T. Hoshi, T. Suzuki and H. Hagiwara, *Mol. Diversity*, 2005, **9**, 317–320, DOI: **10.1007/s11030-005-8107-0**.

58 J. van Schijndel, L. A. Canalle, D. Molendijk and J. Meuldijk, *Green Chem. Lett. Rev.*, 2017, **10**, 404–411, DOI: **10.1080/17518253.2017.1391881**.

59 G. Thirupathi, M. Venkatanarayana, P. K. Dubey and Y. B. Kumari, *Org. Chem. Int.*, 2012, **2012**, 191584, DOI: **10.1155/2012/191584**.

60 G. Kaupp, M. R. Naimi-Jamal and J. Schmeyers, *Tetrahedron*, 2003, **59**, 3753–3760, DOI: **10.1016/S0040-4020(03)00554-4**.

61 C. Peyrot, A. A. M. Peru, L. M. M. Mouterde and F. Allais, *ACS Sustainable Chem. Eng.*, 2019, **7**, 9422–9427, DOI: **10.1021/acssuschemeng.9b00624**.

62 B. Rioux, C. Peyrot, M. M. Mention, F. Brunissen and F. Allais, *Antioxidants*, 2020, **9**, 331, DOI: **10.3390/antiox9040331**.

63 M. D. Horbury, L. A. Baker, N. D. N. Rodrigues, W.-D. Quan and V. G. Stavros, *Chem. Phys. Lett.*, 2017, **673**, 62–67, DOI: **10.1016/j.cplett.2017.02.004**.

64 S. E. Greenough, M. D. Horbury, J. O. F. Thompson, G. M. Roberts, T. N. V. Karsili, B. Marchetti, D. Townsend and V. G. Stavros, *Phys. Chem. Chem. Phys.*, 2014, **16**, 16187–16195, DOI: **10.1039/C4CP02424A**.

65 S. E. Greenough, G. M. Roberts, N. A. Smith, M. D. Horbury, R. G. McKinlay, J. M. Żurek, M. J. Paterson, P. J. Sadler and V. G. Stavros, *Phys. Chem. Chem. Phys.*, 2014, **16**, 19141–19155, DOI: **10.1039/C4CP02359E**.

66 M. P. Grubb, A. J. Orr-Ewing and M. N. R. Ashfold, *Rev. Sci. Instrum.*, 2014, **85**, 064104, DOI: **10.1063/1.4884516**.

67 J. J. Snellenburg, S. Laptenok, R. Seger, K. M. Mullen and I. H. M. van Stokkum, *J. Stat. Software*, 2012, **49**, 1–22, DOI: **10.18637/jss.v049.i03**.

68 K. M. Mullen and I. H. M. van Stokkum, *J. Stat. Software*, 2007, **18**, 1–46, DOI: **10.18637/jss.v018.i03**.

69 S. Chaudhary, H. Lu, A. M. Müller, C. J. Bardeen and M. Ozkan, *Nano Lett.*, 2007, **7**, 1973–1979, DOI: **10.1021/nl070717l**.

70 M. Theelen, K. Bakker, H. Steijvers, S. Roest, P. Hielkema, N. Barreau and E. Haverkamp, *JoVE*, 2018, e55897, DOI: **10.3791/55897**.

71 R. E. van Oustersterp, K. J. Houthuijs, G. Berden, U. F. Engelke, L. A. J. Kluijtmans, R. A. Wevers, K. L. M. Coene, J. Oomens and J. Martens, *Int. J. Mass Spectrom.*, 2019, **443**, 77–85, DOI: **10.1016/j.ijms.2019.05.015**.

72 R. E. van Oustersterp, U. F. H. Engelke, J. Merx, G. Berden, M. Paul, T. Thomulka, A. Berkessel, M. C. D. G. Huigen, L. A. J. Kluijtmans, J. Mecinović, F. P. J. T. Rutjes, C. D. M. van Karnebeek, R. A. Wevers, T. J. Boltje, K. L. M. Coene, J. Martens and J. Oomens, *Anal. Chem.*, 2021, **93**, 15340–15348, DOI: **10.1021/acs.analchem.1c02896**.

73 J. Martens, G. Berden, C. R. Gebhardt and J. Oomens, *Rev. Sci. Instrum.*, 2016, **87**, 103108, DOI: **10.1063/1.4964703**.

74 G. Berden, M. Derksen, K. J. Houthuijs, J. Martens and J. Oomens, *Int. J. Mass Spectrom.*, 2019, **443**, 1–8, DOI: **10.1016/j.ijms.2019.05.013**.

75 G. J. Myatt, E. Ahlberg, Y. Akahori, D. Allen, A. Amberg, L. T. Anger, A. Aptula, S. Auerbach, L. Beilke, P. Bellion, R. Benigni, J. Bercu, E. D. Booth, D. Bower, A. Brigo, N. Burden, Z. Cammerer, M. T. D. Cronin, K. P. Cross, L. Custer, M. Dettwiler, K. Dobo, K. A. Ford, M. C. Fortin, S. E. Gad-McDonald, N. Gellatly, V. Gervais, K. P. Glover, S. Glowienke, J. Van Gompel, S. Gutsell, B. Hardy, J. S. Harvey, J. Hillegass, M. Honma, J.-H. Hsieh, C.-W. Hsu, K. Hughes, C. Johnson, R. Jolly, D. Jones, R. Kemper, M. O. Kenyon, M. T. Kim, N. L. Kruhlak, S. A. Kulkarni, K. Kümmerer, P. Leavitt, B. Majer, S. Masten, S. Miller, J. Moser, M. Mumtaz, W. Muster, L. Neilson, T. I. Oprea, G. Patlewicz, A. Paulino, E. Lo Piparo, M. Powley, D. P. Quigley, M. V. Reddy, A.-N. Richarz, P. Ruiz, B. Schilter, R. Serafimova, W. Simpson, L. Stavitskaya, R. Stidl, D. Suarez-Rodriguez, D. T. Szabo, A. Teasdale, A. Trejo-Martin, J.-P. Valentin, A. Vuorinen, B. A. Wall, P. Watts, A. T. White, J. Wichard, K. L. Witt, A. Woolley, D. Woolley, C. Zwickl and C. Hasselgren, *Regul. Toxicol. Pharmacol.*, 2018, **96**, 1–17, DOI: **10.1016/j.yrtph.2018.04.014**.

76 H. Raunio, *Front. Pharmacol.*, 2011, **2**, 33, DOI: **10.3389/fphar.2011.00033**.

77 VEGA, **https://www.vegahub.eu/portfolio-item/vega-qsar/**, 2022.

78 TEST, **https://www.epa.gov/chemical-research/toxicity-estimation-software-tool-test**, 2022.

79 LAZAR, **https://lazar.in-silico.ch/predict**, 2022.

80 J. Glück, T. Buhrke, F. Frenzel, A. Braeuning and A. Lampen, *Food Chem. Toxicol.*, 2018, **116**, 298–306, DOI: **10.1016/j.fct.2018.04.024**.

81 F. Frenzel, T. Buhrke, I. Wenzel, J. Andrack, J. Hielscher and A. Lampen, *Arch. Toxicol.*, 2017, **91**, 3157–3174, DOI: **10.1007/s00204-016-1924-3**.

82 ISIDA/Predictor, **https://infochim.u-strasbg.fr/cgi-bin/predictor_reach.cgi**, 2022.

83 C. Ortiz, M. L. Ferreira, O. Barbosa, J. C. S. dos Santos, R. C. Rodrigues, Á. Berenguer-Murcia, L. E. Briand and R. Fernandez-Lafuente, *Catal. Sci. Technol.*, 2019, **9**, 2380–2420, DOI: **10.1039/C9CY00415G**.

84 D. Remonatto, R. H. Miotti Jr, R. Monti, J. C. Bassan and A. V. de Paula, *Process Biochem.*, 2022, **114**, 1–20, DOI: **10.1016/j.procbio.2022.01.004**.

85 K. Nasr, A. Favrelle-Huret, R. Mincheva, G. Stoclet, M. Bria, J.-M. Raquez and P. Zinck, *ACS Appl. Polym. Mater.*, 2022, **4**, 1387–1400, DOI: **10.1021/acsapm.1c01777**.

86 A. Siller, S. C. Blaszak, M. Lazar and E. Olasz Harken, *Plast. Surg. Nurs.*, 2018, **38**, 158–161, DOI: **10.1097/PSN.0000000000000244**.

87 P. Sinha Roy, M. M. Mention, M. A. P. Turner, F. Brunissen, V. G. Stavros, G. Garnier, F. Allais and K. Saito, *Green Chem.*, 2021, **23**, 10050–10061, DOI: **10.1039/D1GC02957F**.

88 M. D. Horbury, M. A. P. Turner, J. S. Peters, M. Mention, A. L. Flourat, N. D. M. Hine, F. Allais and V. G. Stavros, *Front. Chem.*, 2020, **8**, 633, DOI: **10.3389/fchem.2020.00633**.

89 C. Waszczak, M. Carmody and J. Kangasjärvi, *Annu. Rev. Plant Biol.*, 2018, **69**, 209–236, DOI: **10.1146/annurev-arplant-042817-040322**.

90 T. Karuppanapandian, J.-C. Moon, C. Kim, K. Manoharan and W. Kim, *Aust. J. Crop Sci.*, 2011, **5**, 709–725.

91 C. Sánchez-Moreno, J. A. Larrauri and F. Saura-Calixto, *J. Sci. Food Agric.*, 1998, **76**, 270–276, DOI: **10.1002/(SICI)1097-0010(199802)76:2<270::AID-JSFA945>3.0.CO;2-9**.

92 J. Luo, Y. Liu, S. Yang, A. L. Flourat, F. Allais and K. Han, *J. Phys. Chem. Lett.*, 2017, **8**, 1025–1030, DOI: **10.1021/acs.jpclett.7b00083**.

93 X. Zhao, J. Luo, S. Yang and K. Han, *J. Phys. Chem. Lett.*, 2019, **10**, 4197–4202, DOI: **10.1021/acs.jpclett.9b01651**.

94 X. Zhao, J. Luo, Y. Liu, P. Pandey, S. Yang, D. Wei and K. Han, *J. Phys. Chem. Lett.*, 2019, **10**, 5244–5249, DOI: **10.1021/acs.jpclett.9b02175**.

95 T. T. Abiola, N. Auckloo, J. M. Woolley, C. Corre, S. Poigny and V. G. Stavros, *Molecules*, 2021, **26**, 7631, DOI: **10.3390/molecules26247631**.

96 X. Zhao, F. Ji, Y. Liang, P. Li, Y. Jia, X. Feng, Y. Sun, Y. Shi, L. Zhu and G. Zhao, *J. Lumin.*, 2020, **223**, 117228, DOI: **10.1016/j.jlumin.2020.117228**.

97 T. T. Abiola, J. M. Toldo, M. T. do Casal, A. L. Flourat, B. Rioux, J. M. Woolley, D. Murdock, F. Allais, M. Barbatti and V. G. Stavros, *Commun. Chem.*, 2022, **5**, 141, DOI: **10.1038/s42004-022-00757-6**.

98 M. J. A. Vink, J. J. Schermer, J. Martens, W. J. Buma, G. Berden and J. Oomens, *ACS Agric. Sci. Technol.*, 2023, **3**, 171, DOI: **10.1021/acsagscitech.2c00279**.

99 J. J. Calvete, P. Juárez and L. Sanz, *J. Mass Spectrom.*, 2007, **42**, 1405–1414, DOI: **10.1002/jms.1242**.

100 E. A. da Silva-Junior, C. R. Paludo, D. R. Gouvea, M. J. Kato, N. A. J. C. Furtado, N. P. Lopes, R. Vessecchi and M. T. Pupo, *J. Mass Spectrom.*, 2017, **52**, 517–525, DOI: **10.1002/jms.3955**.

101 M. J. A. Vink, F. A. M. G. van Geenen, G. Berden, T. J. C. O'Riordan, P. W. A. Howe, J. Oomens, S. J. Perry and J. Martens, *Environ. Sci. Technol.*, 2022, **56**, 15563–15572, DOI: **10.1021/acs.est.2c03210**.

102 M. A. Duncan, *J. Phys. Chem. A*, 2012, **116**, 11477–11491, DOI: **10.1021/jp309037d**.

103 O. Dopfer, *Int. Rev. Phys. Chem.*, 2003, **22**, 437–495, DOI: **10.1080/0144235031000112878**.

104 A. L. Nicely, D. J. Miller and J. M. Lisy, *J. Am. Chem. Soc.*, 2009, **131**, 6314–6315, DOI: **10.1021/ja8094526**.

105 E. J. Bieske and O. Dopfer, *Chem. Rev.*, 2000, **100**, 3963–3998, DOI: **10.1021/cr990064w**.